

1
2
3
4
5
6
7
8
9
10
11
12
13
14
15
16
17
18
19
20
21
22
23

A reduced order computational model of a semi-active variable-stiffness foot prosthesis

Michael A. McGeehan, MS¹; Peter G. Adamczyk, PhD²; Kieran M. Nichols, MS²; Michael E. Hahn, PhD¹

Institutional Affiliations

¹University of Oregon Department of Human Physiology
181 Esslinger Hall, 1525 University St.
Eugene, OR 97403

mmcgeeha@uoregon.edu, mhahn@uoregon.edu

²University of Wisconsin-Madison Department of Mechanical Engineering
Room 3039, Mechanical Engineering Building
1513 University Ave.
Madison, WI 53706-1539

peter.adamczyk@wisc.edu, knichols4@wisc.edu

Corresponding Author Information

Michael E. Hahn, PhD
University of Oregon, 181 Esslinger Hall, 1525 University St.
Eugene, OR 97403
(541) 346-3554
mhahn@uoregon.edu

24 **Introduction:** Passive energy storage and return (ESR) feet are the current performance standard in lower limb
25 prostheses. A recently developed semi-active variable-stiffness foot (VSF) prosthesis balances the simplicity of a
26 passive ESR device with the adaptability of a powered design. The purpose of this study was to model and simulate
27 the ESR properties of the VSF prosthesis. **Methods:** The ESR properties of the VSF were modeled as a lumped
28 parameter overhung beam. The overhung length is variable, allowing the model to exhibit variable ESR stiffness.
29 Foot-ground contact was modeled using sphere-to-plane contact models. Contact parameters were optimized to
30 represent the geometry and dynamics of the VSF and its foam base. Static compression tests and gait were
31 simulated. Simulation outcomes were compared to corresponding experimental data. **Results:** Stiffness of the model
32 matched that of the physical VSF (R^2 : 0.98, RMSE: 1.37 N/mm). Model-predicted resultant ground reaction force
33 (GRF_r) matched well under optimized parameter conditions (R^2 : 0.98, RMSE: 5.3% body weight,) and unoptimized
34 parameter conditions (R^2 : 0.90, mean RMSE: 13% body weight). Anterior-posterior center of pressure matched well
35 with $R^2 > 0.94$ and RMSE $< 9.5\%$ foot length in all conditions. **Conclusions:** The ESR properties of the VSF were
36 accurately simulated under benchtop testing and dynamic gait conditions. These methods may be useful for
37 predicting GRF_r arising from gait with novel prostheses. Such data are useful to optimize prosthesis design
38 parameters on a user-specific basis.

39 1. Introduction

40 Individuals with lower limb loss exhibit distinct gait characteristics, which may limit mobility and decrease
41 quality of life. Those using lower limb prostheses may display gait asymmetry [1,2], elevated metabolic cost during
42 locomotion [3], and a variety of psychological disorders including anxiety and depression [4]. Sustained prosthesis
43 use may also induce overloading of intact joints and ultimately, musculoskeletal ailments [5]. Each of these issues
44 may be attenuated by improving user specificity in the design characteristics of foot prostheses. However, the effects
45 of foot prosthesis design parameters (e.g. stiffness) are not well characterized, and thus achieving meaningful
46 improvements in gait has proven arduous [6,7]. In order to achieve improvements, a robust understanding of the
47 relationships between anthropometry, gait mechanics, and prosthesis design are necessary.

48 One of the primary design goals of a lower limb prosthesis is to replace the coordinated energy absorption and
49 generation properties of a lost limb. Passive energy storage and return (ESR) foot prostheses are the current standard
50 for mimicking this functionality. However, the fixed stiffness behavior of these devices contrasts that of the healthy
51 foot-ankle complex, which modulates its behavior in response to varied gait conditions (e.g. velocity and terrain)
52 [8,9]. Glanzer and Adamczyk (2018) [10] recently developed a variable-stiffness foot (VSF) prosthesis designed
53 with an actuated keel support fulcrum to semi-actively control sagittal forefoot stiffness and thereby adapt to
54 different gait conditions with low power (Fig. 1). The ESR keel of the VSF is a composite leaf spring designed as an
55 overhung beam, which modulates the supported length (l) via an actuated keel support fulcrum (B). The total beam
56 length (L) is 229 mm, whereas the overhung length (a) is variable between 66–151 mm. By modulating overhung
57 length, the VSF's forefoot is capable of exhibiting roughly a three-fold range of forefoot stiffness values (10–32
58 N/mm). The heel component of the VSF has a consistent linear stiffness of 65 N/mm. The VSF's fulcrum position is
59 designed to be adjusted during swing phase, thus minimizing the power necessary for actuation. As such, the VSF
60 behaves primarily as a passive ESR prosthesis, which can adapt stiffness in response to variable gait conditions.

61 Simulations based on computational models can be powerful tools for evaluating potential biomechanical
62 interventions, such as the implementation of a novel ESR prosthesis. Recently, simulations have been used to aid in
63 the iterative design process and improve user-specificity [11–13]. Inverse simulations provide the ability to estimate
64 values that cannot be measured *in vivo* (e.g. socket-residual limb interface dynamics), whereas predictive
65 simulations suggest hypotheses regarding how humans may interact with and adapt to new prosthetic devices.

66 Computational modeling has been used to investigate the effects of prosthesis alignment [14] and a biarticular
67 clutched spring mechanism [15] on gait mechanics among persons with lower limb loss. However, these models do
68 not account for the ESR properties of the prosthetic foot, thus limiting their ecological validity. Other studies, which
69 did incorporate the force and torque contributions of ESR feet into gait models focused on characterizing
70 biomechanical and myo physiologic responses with prosthesis use, rather than validation of the prosthesis model
71 [16,17]. While these studies made important progress toward investigating the relationship between anthropometry,
72 gait mechanics, and prosthetic foot design, they had limited ability to verify simulation results in the context of
73 experimental values. Due to these limitations, the use of simulations to inform the design of ESR foot prostheses has
74 not been fully realized. The purpose of this study was to further couple experimental and simulation prosthesis data
75 by modeling and validating the mechanical stiffness properties and resulting ground reaction forces of a semi-active
76 VSF.

77 2. Methods

78 2.1 Model design

79 A computational model of the VSF was developed in Simscape Multibody (Mathworks, Inc., Natick, MA).
80 The assembly, geometry, mass, and inertial properties were derived from SolidWorks (Dassault Systemes Inc.,
81 Waltham, MA). A reduced order model of the VSF's variable-stiffness elastic keel was designed using the lumped
82 parameter approach for approximating flexible body dynamics. This approach involved discretizing the continuous
83 geometry of the keel into finite rigid segments coupled via revolute joints, springs, and dampers (Fig. 2). This
84 simplification of the original state space of the continuous elastic keel system to finite dimensions allows the partial
85 differential equations of the infinite-dimensional time-space states of the physical VSF to be represented by ordinary
86 differential equations with a finite number of parameters.

87 The keel of the VSF model was discretized into 16 segments (eight DoF). The most posterior segment is 66
88 mm in length, which matches the minimum possible fulcrum position. The rest of the keel consists of 11.64-mm
89 segments for a total beam length of 229 mm (Fig. 2). The stiffness and damping values for the revolute joints were
90 parameterized to represent the material properties of the VSF's G10/FR4 Garolite keel (flexural elastic modulus:
91
92

18.6 GPa, Poisson's ratio: 0.136). A MATLAB script controls continuous fulcrum position (i.e. variable stiffness). The VSF model was rigidly attached to a prosthetic pylon and socket via a pyramid adapter, as the device would be used *in vivo*. These connections were modeled as weld joints. Each segment is independently scalable, allowing the model to be integrated into an anatomically scaled computational gait model.

Foot-ground contact consists of 24 sphere-to-plane contact models [18] parameterized to represent the geometry and dynamics of the VSF's foam base. Each of these models estimates normal (F_n) and frictional (F_f) forces associated with the collision of a viscoelastic sphere (a massless spring and damper system) and a rigid plane (Fig. 3). The overall foot contact model was divided into five zones; the sphere-to-plane models were parameterized by zone (Fig. 3, Table 1). The heel of the VSF model is comprised of three zones; this choice was motivated by the sensitivity of contact parameters when few spheres are in contact with the walking plane (e.g. the heel of the foot early in stance phase). Contact parameters are less sensitive when many spheres are in contact with the walking plane (e.g. the midfoot and forefoot late in stance phase). The foam base of the physical VSF undergoes compression throughout stance phase. To account for these effects, a modified Kelvin-Voigt nonlinear spring and damper force law (eq. (1)) was implemented to represent contact between the VSF and walking plane:

$$F_n = \begin{cases} (k \times \delta^n) + y(b \times \dot{\delta}) & \delta > 0, \dot{\delta} > 0 \\ k \times \delta & \delta > 0, \dot{\delta} < 0 \\ 0 & \delta < 0 \end{cases} \quad (1)$$

F_n : normal force

k : contact stiffness

δ : penetration depth

n : penetration exponent

y : damping force scaling factor

b : contact damping coefficient

The spring force increases exponentially as the sphere penetrates the contact plane. The damping force is multiplied by a scaling factor (y), which increases from zero to one as a polynomial as it approaches a user-defined value for full damping. Frictional force (eq. (2)) is the product of the normal force and coefficient of friction (μ). A stick-slip friction law defines the transition between static (μ_{static}) and kinetic ($\mu_{kinetic}$) coefficients of friction based on a velocity threshold ($v_{threshold}$):

$$F_f = \begin{cases} F_n \times \mu_{static} & v_{poc} < v_{threshold} \\ F_n \times \mu_{kinetic} & v_{poc} > v_{threshold} \end{cases} \quad (2)$$

F_f : frictional force

μ : coefficient of friction

v_{poc} : velocity at point of contact

$v_{threshold}$: velocity threshold

Static and kinetic coefficients of friction were set to 0.5 and 0.3 with a velocity threshold of 0.1 m/s. Resultant ground reaction force (GRF_{*x*}) was derived by summing and low-pass filtering (4th order Butterworth, f_c : 40 Hz) the normal and frictional forces arising from each contact sphere.

In order to improve GRF_{*x*} predictions, contact model parameterization was formulated as a least-squares optimization problem with the objective of minimizing the sum of squared errors between model-predicted and experimentally measured GRF_{*x*} (see "Model Validation"). Initial parameter settings at the outset of the optimization were derived by increasing stiffness until the contact spheres were able to support the weight of the model. Initial damping coefficients (N·s/mm) were set to half the numerical value of stiffness (N/mm). Penetration exponents and penetration for full damping values were initialized at 1 and 1 mm, respectively. These initial values were used as inputs to the problem. Latin hypercube sampling (LHS) was applied to generate simulation scenarios with pseudo-random sets of parameters. The LHS approach is a method of stratified sampling, which divides parameter values into equal strata based on an assumed normal distribution and constrained by user-defined bounds. Random parameter values are sampled from within these strata to generate a simulation scenario with a pseudo-random set of parameters. The LHS technique effectively samples the search space, while providing the randomness required to explore the efficacy of a range of variable values to minimize the objective function. The objective function value of each iteration is compared to the previous iteration; the parameter scenario which best minimizes the objective is passed to the next iteration of the algorithm. The optimization algorithm proceeds for 100 iterations or until an

145 objective function tolerance of 0.1 N is reached (i.e. convergence). If the optimization algorithm did not meet any of
 146 the termination criteria, the initial parameter values were updated using the results of the first run, and an additional
 147 run was initiated. Parameter tolerances were set to 0.001 (varying units) in order to avoid false minima.

148 2.2 Model validation

149 2.2.1 *Static compression testing*

150
 151 The operational stiffness range of the physical VSF was determined through static compression testing
 152 (TestResources, Shakopee, MN) (Glanzer and Adamczyk 2018). Load was applied at a constant speed of 50
 153 mm/min to a point 30 mm proximal to the anterior tip of the VSF (i.e. supported beam length = 199 mm). To
 154 validate the ESR properties of the VSF model, a simulated materials testing system (MTS) was developed in
 155 Simscape Multibody. The MTS simulator consists of a massless body, which translates vertically according to a
 156 user-defined time-position vector (Fig. 2). Simulated static compression tests were performed as in Glanzer and
 157 Adamczyk (2018). Contact was maintained throughout VSF deflection. Contact dynamics between the VSF and
 158 MTS were estimated using a sphere-to-sphere contact model. Stiffness (k) (eq. (3)) was computed as the average
 159 slope of the load-displacement data for loads above 200 N.
 160
 161

$$162 \quad k = \frac{\Delta_{\text{Load}}}{\Delta_{\text{Displacement}}} \text{ for loads } 200 \text{ N to } F_{\text{max}} \quad (3)$$

163
 164 Deformation for loads under 200 N was considered to arise primarily from foam compression, rather than keel
 165 displacement. Mid-range keel displacement was also calculated for the VSF model as the displacement of the keel at
 166 50 percent of the maximal load applied during the static compression test.

167 Static compression tests were simulated at five discrete fulcrum positions (66, 87, 108, 129, and 151 mm),
 168 which span the full continuous range of possible positions. Simulation-derived values were compared to those from
 169 static compression tests of the physical VSF via coefficient of determination and root mean squared error (RMSE).
 170 Simulations were calculated in Simscape Multibody using the *ode15s* solver profile with variable step size.
 171

172 2.2.2 *Gait conditions*

173 Model-predicted GRF_x was validated under two scenarios: static and dynamic gait conditions. For both
 174 validations, the VSF model was integrated into a seven-segment, 28-DoF anatomically-scaled gait model of a
 175 subject with a unilateral transtibial amputation. Three-dimensional optical motion capture data (Optitrack, Natural
 176 Point, Inc. Corvallis, OR) of a male subject (181 cm, 78.0 kg) with a right side transtibial amputation walking with
 177 the physical VSF were used as inputs to the model. Retroreflective marker coordinates from a static motion capture
 178 trial were used to estimate and scale limb dimensions for the pelvis, leg, intact shank, residual shank, and intact foot.
 179 Within the gait model, the residual shank was encapsulated in a prosthetic socket and welded to the pyramid adapter
 180 of the VSF model (Fig. 2). The interface between the prosthetic socket and residual limb was modeled as a high-
 181 stiffness 6-DoF bushing joint, similar to previous work by LaPrè et al. (2018). The rotational and translational
 182 stiffness as well as displacement and velocity constraints were designed according to previous gait experiments [19]
 183 and finite element analysis [20]. The mass and inertial properties of the lower limbs and pelvis were modeled as
 184 conical frusta and an ellipsoid, respectively. Segment masses were estimated according to De Leva (1996).

185 For the static condition, the model was simulated with anatomically neutral joint angles for ten seconds. Model-
 186 predicted GRF_x was averaged over the course of the trial and compared to the mass of the subject. Dynamic gait
 187 simulations were calculated based on experimental motion capture trials of the subject walking over ground between
 188 1.0 and 1.2 m/s with the VSF under low, medium and high stiffness configurations (fulcrum positions: 66, 108, and
 189 151 mm). Three trials were collected for each stiffness configuration for a total of nine trials. Three-axis pelvis, hip,
 190 knee, and ankle angles were calculated from three-dimensional marker coordinate data [22,23] and used as inputs to
 191 drive the corresponding joints of the model. Motion at the socket-limb interface was considered to be passive based
 192 on the aforementioned velocity and displacement constraints. The pyramid adapter-pylon interface was assumed to
 193 be rigid.

194 Contact model-derived GRF_x prediction was optimized for a single trial at the 66-mm fulcrum position. The
 195 GRF_x error resulting from this trial represents the theoretical optimal performance of the comprehensive VSF-ground
 196 contact model. The transferability of the optimized parameter values was determined by simulating the two
 197 remaining low stiffness trials and the three remaining trials each for the medium and high stiffness configurations.

198 Joint kinematics and GRF_x data were low-pass filtered (4th order Butterworth; f_c : 6 Hz and 40 Hz,
 199 respectively). Simulation and experimental GRF_x were time locked and indexed to 0.25 s before and 0.25 s after

200 stance phase. Including the brief period before and after stance phase provides insights regarding how the contact
 201 model behaves outside of stance phase and whether or not key gait events (e.g. heel strike and toe off) occur at
 202 similar time points in the simulated and experimental data. Resultant ground reaction force time series were re-
 203 sampled to 101 data points via cubic spline interpolation to allow for comparison between stance phases of differing
 204 lengths. Ensemble curves (mean \pm SD) were generated for each condition. The impulse of GRF_k was calculated to
 205 assess the simulation's ability to predict GRF_k trajectory.

206 Anterior-posterior center of pressure (CoP_{AP}) position was calculated as the weighted sum of each contact
 207 sphere's predicted force multiplied by its anterior-posterior position (x). Raw normal forces arising from each sphere
 208 during stance phase were low-pass filtered (4th order Butterworth; f_c : 40 Hz) and summed. Anterior-posterior CoP
 209 position was calculated across stance phase (eq. (4)).
 210

$$211 \quad CoP_{AP} = \frac{\sum_{i=1}^N x_i F_{n_i}}{\sum F_n} \quad (4)$$

212 **CoP_{AP}**: Anterior-posterior center of pressure position

213 x : Anterior posterior coordinate of contact sphere

214

215 The CoP_{AP} time series data were low-pass filtered (4th order Butterworth; f_c : 6 Hz) and re-sampled to 101 data points
 216 via cubic spline interpolation to allow for comparison between stance phases of differing lengths. Joint kinematics,
 217 GRF_k , and CoP_{AP} data measured during experimental gait trials were compared to those derived from the simulations
 218 using coefficient of determination and RMSE.

219

220 3. Results

221

222 3.1 Static compression tests

223 Simulated VSF stiffness effectively reproduced experimental stiffness across the five fulcrum
 224 configurations ($R^2 > 0.98$, RMSE = 1.37 N/mm) (Fig. 4, Table 2). Simulated mid-range displacement also matched
 225 well ($R^2 > 0.99$) with small offset from experimental displacement in each condition (RMSE = 0.45 mm).
 226 Experimental load-displacement relationships were most linear in the 66 and 87 mm fulcrum configurations, as
 227 indicated by variance in the slope of the relationship. The stiffest three conditions exhibited curvilinear relationships.
 228 Simulated load-displacement data were linear in all conditions due to the linear spring and damper force parameters
 229 for the revolute joints in the lumped parameter keel model.
 230

231 3.2 Resultant ground reaction force predictions

232 In the static condition, model-predicted subject mass was $2.6 \pm 0.0\%$ less than measured mass. In the
 233 dynamic conditions, simulated joint angles matched experimental joint angles well, but exhibited a small phase lag
 234 (mean RMSE: 1.9 ± 1.0 deg, mean R^2 : 0.98 ± 0.02). Simulated and experimental GRF_k data agreed well in the time
 235 domain (Fig. 6). Amplitude discrepancies, quantified via RMSE, were least in low stiffness configuration and
 236 greatest in the high stiffness configuration. Coefficient of determination values were similar for the low and medium
 237 stiffness conditions and lower for the high stiffness condition. Impulse was similar in the low and high stiffness
 238 conditions and lower for the medium stiffness condition (Table 3).
 239

240 Optimization of the single low stiffness trial resulted in a GRF_k RMSE of 5.3% body weight (BW) and R^2 of
 241 0.98 across stance phase. Impulse also matched well (RMSE: 0.01 BW·s, $R^2 > 0.99$) (Fig. 5). In the time domain,
 242 model-predicted heel contact preceded experimental heel contact by 0.02 s, resulting in a 0.02-s longer stance phase.
 243 Simulating the two additional low stiffness trials with the optimized contact parameters resulted in average RMSE
 244 and R^2 values of 0.10 ± 0.05 BW and 0.93 ± 0.05 for GRF_k and 0.02 ± 0.01 BW·s and $> 0.99 \pm 0.01$ for GRF_k
 245 impulse (Fig. 6, Table 3).

246 Experimental GRF_k and GRF_k impulse responses were similar in the time and amplitude domains across the
 247 three stiffness conditions (Fig. 6). On average, stance phase time was 0.05 ± 0.03 s longer in the simulations across
 248 the stiffness conditions. Time errors were least in the low stiffness condition and greatest in the high stiffness.
 249 Variability for GRF_k was greatest during the first 25% of stance phase for all conditions. Variability for GRF_k
 250 impulse was greatest near the end of stance phase. The ability of the contact parameters optimized for the low
 251 stiffness condition transferred well across the other two conditions, which is evident by the similar RMSE values for
 252 GRF_k (Table 3). Resultant ground reaction force RMSE and R^2 values were better in the medium stiffness
 253 configuration, whereas RMSE and R^2 were better in the high stiffness condition for GRF_k impulse. The medium
 254 stiffness condition demonstrated the least variability for the GRF_k response, whereas the low and high stiffness
 conditions showed similarly low variability for GRF_k impulse (Table 3).

Anterior-posterior CoP trajectory during stance phase was similar between simulated and experimental data (Fig. 7). Root mean squared errors were 8.9 ± 1.0 , 9.5 ± 0.9 , and 5.7 ± 1.4 percent foot length for the low, medium, and high stiffness conditions, respectively (Table 3). Simulated data correlated well with experimental data across all conditions. Coefficient of determination values were 0.95 ± 0.01 , 0.94 ± 0.01 , and 0.97 ± 0.01 for the low, medium, and high stiffness conditions.

4. Discussion

The goal of this study was to develop a reduced-order computational model of a semi-active variable-stiffness foot prosthesis. Results from simulated static compression tests showed good agreement with experimental data. These outcomes suggest that the variable-stiffness ESR properties of the VSF were modeled with high fidelity using a reduced order lumped parameter approach for approximating flexible body dynamics. One of the goals of reduced order modeling is to capture a structure's dynamic behavior in a computationally inexpensive way. A common benchmark for reduced-order models is the ability to simulate at or near real-time [24,25], which contrasts with more computationally expensive methods such as mesh-based finite element modeling. Including initialization time, static compression simulations computed 3.3 ± 0.8 times faster than real-time (i.e. the length of time required to complete the experimental static compression test) on computer with a four core 4.0 GHz processor. Initialization time, which includes model compiling and building, can be minimized using "Accelerator" and "Fast Restart" modes in Simscape Multibody. Using these tools, simulations computed 39 ± 16 times faster than real time. This computational efficiency is useful if the model is to be simulated iteratively, for example in parameter optimization or machine learning frameworks.

The range of forefoot stiffness values exhibited by the physical VSF and captured by the VSF model represent a range of stiffness values available in many commercially-available prosthetic feet [26,27]. Accurate characterization of this range is important, should this model be used to inform the design and/or prescription of prosthetic feet. Further, this model can be easily re-parameterized to exhibit a different range of stiffness values, which could aid in the selection of keel dimensions or material properties to meet design goals. Two primary limitations are present for the static compression testing simulations. Experimental load-displacement data were only available for positive loading conditions, and thus a comparison of the model's hysteresis behavior was not possible. Similarly, experimental data were only available for the 50 mm/min loading rate. A robust characterization of the VSF's stiffness behavior under a range of loading rates would likely improve the model's behavior under dynamic conditions. Experimental load-displacement data could also be influenced by imperfections in maintaining a constant contact point with the prosthesis.

Under dynamic gait conditions, simulated joint angles agreed well with experimental values, indicating that the model is numerically stable when actuated by joint kinematics measured during gait with the VSF. Joint angles were strongly correlated, but exhibited a small phase lag, possibly due to ODE solver settings and numerical integration. This phase lag may be also be present in the kinetic data, but masked by the larger inherent variability of the simulated GRF_x. Total simulation times were 8.95 ± 3.92 , 12.7 ± 0.67 , and 46.2 ± 1.19 times slower than real time for the low, medium, and high stiffness configurations respectively. Execution times were 3.12 ± 0.10 , 3.40 ± 0.67 , and 38.4 ± 1.19 times slower than real time. Increased execution times for the stiff conditions may reflect the need for small time-steps in solving a rapidly-evolving, stiff differential equation.

Optimization of the GRF_x for the low stiffness configuration achieved a RMSE of 5.3% BW and R² of 0.98. These values are similar to those reported in previous biomechanical contact modeling work [28–30]. However, those studies focused on quantification of foot-ground contact during gait for individuals with intact limbs. Direct comparison of these data was limited to work in intact limb biomechanical modeling due to a lack of studies reporting validation data for prosthesis-ground contact modeling in gait biomechanics. The strong correlation and low error for GRF_x impulse indicates that the contact model is able to predict the shape and trajectory of the GRF_x arising from gait kinematics. Accurate predictions of GRF_x impulse is important for capturing whole-body energetics throughout gait. The concomitant agreement for both kinematics and kinetics further suggests that these methods are viable for simulating whole-body energetics during gait.

The transferability of the optimized contact model parameters from the low stiffness condition was assessed by simulating two additional low stiffness trials and three trials each with medium and high stiffness configurations. Compared to the optimized trial, simulation-derived GRF_x predictions did not perform as well in the unoptimized trials. Mean GRF_x RMSE and R² were $12.7 \pm 1.44\%$ BW and 0.91 ± 0.02 for the remaining low stiffness trials. These values were similar for the medium and low stiffness trials (Table 3). The impulse of these data matched well across the unoptimized trials (RMSE: 0.03 ± 0.02 BW·s, R²: 0.98 ± 0.01). Variability of the model's performance was similar across the unoptimized conditions for all outcome measures. It is possible that the

311 contact model parameters were over-fitted to the specific conditions of a single trial, resulting in decreased
312 generalizability. Future work should assess the balance between optimization specificity and generalizability.

313 The amplitude and shape of experimental GRF_k waveforms were similar across the three stiffness
314 conditions. However, stance phase times did vary by condition for the subject tested. The medium stiffness
315 condition resulted in the longest stance phase time (0.79 ± 0.01 s), high stiffness resulted in the shortest (0.71 ± 0.02
316 s), and low stiffness (0.73 ± 0.02 s) was in the middle. The same pattern was present in the simulated data, although
317 stance phase times were 0.05 ± 0.03 s longer on average compared to the experimental data. Stance phase times
318 derived from simulations were correlated with experimental times ($R^2 = 0.65$). More data are necessary to discern the
319 strength, repeatability, and significance of these relationships.

320 Simulated CoP_{AP} values agreed well with experimental values. The RMSE values achieved using this model
321 were similar to those reported in previous work involving subject-specific biomechanical contact modeling for
322 individuals with intact limbs [31]. Accurate mapping of CoP_{AP} throughout stance phase is vital for simulating the
323 effects of variable prosthesis stiffness on joint forces and moments during gait. Errors in model-predicted CoP_{AP} may
324 be reduced by increasing the density of contact spheres distributed on the plantar surface of the foot, which would
325 improve the resolution of CoP_{AP} predictions. However, this would likely result in increased execution time for
326 simulations and also increase complexity of the contact parameter optimization problem.

327 The present data show promise for predicting GRF_k arising from a semi-active VSF prosthesis. These
328 methods may be applied to the design and prescription of lower limb prostheses and forward dynamics simulations
329 in robotics and biomechanics. Within biomechanics, future work could integrate the VSF model into a gait model of
330 an individual with lower limb loss. Gait simulations could be formulated as an optimal control problem in which
331 prosthesis stiffness is tuned to minimize a biomechanical cost function such as joint loading or metabolic cost.
332 Further optimization of the VSF-ground contact model may be necessary for simulation scenarios with error
333 tolerances less than 12% BW. Similar improvements may be required if the mean difference between simulation
334 conditions is less than the error of the model. Reducing error in model-predicted GRF_k may be accomplished by
335 evaluating the objective function under a variety of conditions and choosing the parameter set that achieves the best
336 minimization across several conditions. A deformable contact model, such as presented in Jackson, Hass, and Fregly
337 (2016), may also be a viable means of representing foam deformation throughout stance phase and thus reducing
338 error.

339 These methods assume accurate estimation of segment length, joint centers, and joint angles which were
340 derived from marker-based motion capture data. Each of these metrics likely suffers from small errors due to marker
341 placement, localization, and coordinate system design. Such errors would contribute to decrements in contact model
342 performance. The components and joints of the prosthetic limb were also modeled as rigid, which may not be
343 completely accurate to represent the physical limb. This discrepancy would manifest as small differences in
344 kinematics and energy transfer between the components of the prosthetic limb. Nevertheless, simulated motions
345 were consistent with experimental data of subjects walking with the VSF and other previously reported data of
346 spatiotemporal gait patterns among persons with lower limb loss [33,34]. Another limitation is inherent to the
347 reduced order design of the lumped parameter VSF keel, which constrains keel motion to the sagittal plane. While
348 this design is computationally efficient compared to more robust finite element models, it fails to account for small
349 torsional keel motions that would be possible under ecological gait conditions with the physical VSF.

350 5. Conclusions

351
352
353 The present study demonstrates that the ESR properties of a semi-active VSF can be modeled with high
354 fidelity. Foot-ground contact models were used to estimate GRF_k with 5.3% BW error in an optimized gait trial,
355 which translated to mean errors of 13% for unoptimized trials. The contact models also predicted CoP_{AP} with mean
356 error of 9.3% foot length. This model performance may be sufficient for gait simulations among persons with lower
357 limb loss. Such simulations may be used to aid in the prosthesis design and prescription process in order to improve
358 user mobility. These methods may also be helpful to identify other important prosthesis design parameters, which
359 can be modified to optimize gait. Further contact model optimization and error reduction may be required for
360 simulation-based comparisons of varied prosthesis stiffness, where differences in GRF_k magnitude may be nuanced.

Statement of acknowledgements

361 **Statement of acknowledgements:** The authors would like to thank Evan Glanzer for his work in developing and
362 testing the variable-stiffness foot and Terry Denery for his intellectual contributions in optimizing the contact model.

363

364 **Funding sources:** This work was funded in part by the Lokey Doctoral Science Fellowship (MAM) and NIH grant
365 HD074424 (PGA).

366

Acronyms widely used in text

BW	Body weight; M*g
CoP	Center of pressure
DoF	Degrees of Freedom
ESR	Energy storage and return
GRF _R	Resultant Ground Reaction Force, N; $\sqrt{GRF_x^2 + GRF_y^2 + GRF_z^2}$
LHS	Latin Hypercube Sampling
MTS	Material Testing System
<i>ode15s</i>	Ordinary differential equation 15 solver
SD	Standard Deviation
RMSE	Root Mean Square Error; $\sqrt{\frac{\sum_{i=1}^N (Experimental_i - Simulation_i)^2}{N}}$
VSF	Variable Stiffness Foot

Abbreviations

<i>a</i>	Overhung length, mm
<i>b</i>	Damping coefficient, N·s/mm
<i>B</i>	Support fulcrum position, mm
<i>D</i>	Displacement, mm
<i>F</i>	Force, N
<i>k</i>	Linear stiffness, N/mm
<i>L</i>	Total beam length, mm
<i>l</i>	Supported length, mm
<i>n</i>	Penetration exponent
<i>R</i> ²	Coefficient of determination
μ	Coefficient of friction
<i>v</i>	Linear velocity
<i>y</i>	Scaling factor
δ	Penetration depth, mm
$\dot{\delta}$	Penetration velocity, mm/s
ω	Angular velocity, rad/s

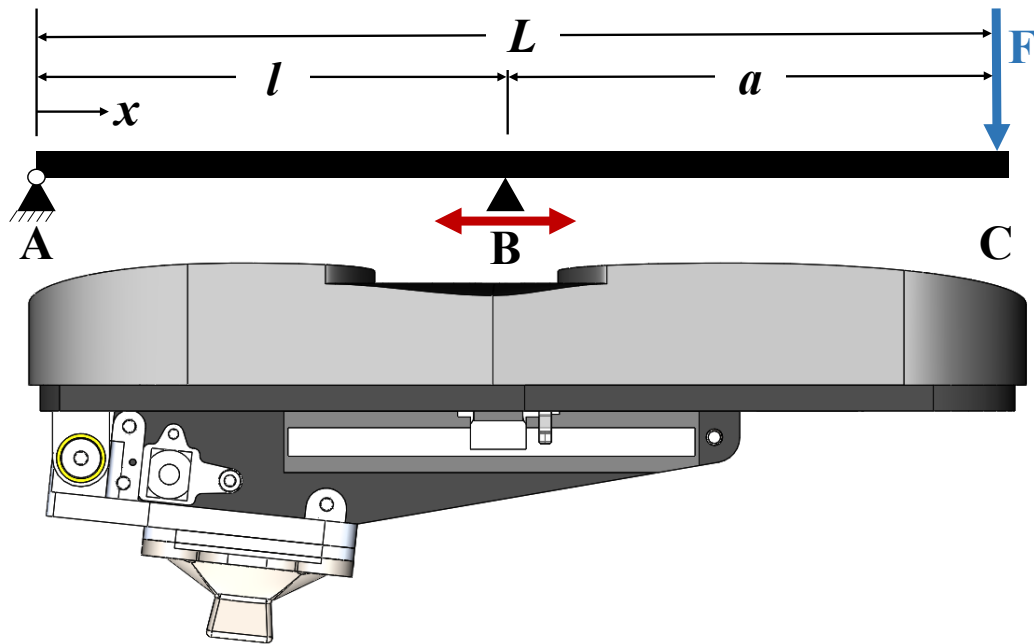
Superscripts and subscripts

CoP _{ap}	Anterior-posterior (Center of Pressure)
<i>D</i> _{sim}	Simulation (Displacement)
<i>D</i> _{ep}	Experimental (Displacement)
<i>F</i> _f	Frictional force, N
<i>F</i> _n	Normal force, N
GRF _R	Resultant ground reaction force, N
<i>k</i> _{sim}	Simulation (stiffness), N/mm
<i>k</i> _{exp}	Experimental (stiffness), N/mm
<i>v</i> _{poc}	Linear velocity at point of contact, mm/s
<i>v</i> _{threshold}	Linear velocity threshold, m/s
μ _{kinetic}	Coefficient of kinetic friction
μ _{static}	Coefficient of static friction

- 369 [1] Schaarschmidt, M., Lipfert, S. W., Meier-Gratz, C., Scholle, H. C., and Seyfarth, A., 2012, "Functional Gait
370 Asymmetry of Unilateral Transfemoral Amputees," *Hum. Mov. Sci.*, **31**(4), pp. 907–917.
- 371 [2] Sanderson, D. J., and Martin, P. E., 1997, "Lower Extremity Kinematic and Kinetic Adaptations in
372 Unilateral Below-Knee Amputees during Walking," *Gait Posture*, **6**(2), pp. 126–136.
- 373 [3] van Schaik, L., Geertzen, J. H., Dijkstra, P. U., and Dekker, R., 2019, "Metabolic Costs of Activities of
374 Daily Living in Subjects with Lower Limb Amputation: A Systematic Review and Meta-Analysis. Article
375 Submitted for Publication," *PLoS One*, **14**(3), p. e0213256.
- 376 [4] Mckechnie, P. S., and John, A., 2014, "Anxiety and Depression Following Traumatic Limb Amputation: A
377 Systematic Review.," *Injury*, **45**(12), pp. 1859–66.
- 378 [5] Gailey, R., Allen, K., Castles, J., Kucharik, J., and Roeder, M., 2008, "Review of Secondary Physical
379 Conditions Associated with Lower-Limb Amputation and Long-Term Prosthesis Use," *JRRD*, **45**(1), pp.
380 15–30.
- 381 [6] Casillas, J. M., Dulieu, V., Cohen, M., Marcer, I., and Didier, J. P., 1995, "Bioenergetic Comparison of a
382 New Energy-Storing Foot and SACH Foot in Traumatic below-Knee Vascular Amputations.," *Arch. Phys.
383 Med. Rehabil.*, **76**(1), pp. 39–44.
- 384 [7] Postema, K., Hermens, H. J., De Vries, J., Koopman, H. F. J. M., and Eisma, W. H., 1997, "Energy Storage
385 and Release of Prosthetic Feet Part 1: Biomechanical Analysis Related to User Benefits," *Prosthet. Orthot.
386 Int.*, **21**, pp. 17–27.
- 387 [8] Farris, D. J., and Sawicki, G. S., 2012, "The Mechanics and Energetics of Human Walking and Running: A
388 Joint Level Perspective," *J. R. Soc. Interface*, **9**, pp. 110–18.
- 389 [9] Winter, D. A., 1983, "Energy Generation and Absorption at the Ankle and Knee during Fast, Natural, and
390 Slow Cadences," *Clin. Orthop. Relat. Res.*, **175**, pp. 147–154.
- 391 [10] Glanzer, E. M., and Adamczyk, P. G., 2018, "Design and Validation of a Semi-Active Variable Stiffness
392 Foot Prosthesis," *IEEE Trans. Neural Syst. Rehabil. Eng.*, **26**(12), pp. 2351–2359.
- 393 [11] Fey, N. P., Klute, G. K., and Neptune, R. R., 2013, "Altering Prosthetic Foot Stiffness Influences Foot and
394 Muscle Function during Below-Knee Amputee Walking: A Modeling and Simulation Analysis," *J.
395 Biomech.*, **46**, pp. 637–644.
- 396 [12] Strbac, M., and Popovic, D., 2012, "Software Tool for the Prosthetic Foot Modeling and Stiffness
397 Optimization," *Comput. Math. Methods Med.*, **2012**.
- 398 [13] Tryggvason, H., Starker, F., Lecomte, C., and Jonsdottir, F., 2020, "Use of Dynamic FEA for Design
399 Modification and Energy Analysis of a Variable Stiffness Prosthetic Foot," *Appl. Sci.*, **10**(2), p. 650.
- 400 [14] Laprè, A. K., Umberger, B. R., and Sup, F., 2014, "Simulation of a Powered Ankle Prosthesis with Dynamic
401 Joint Alignment," *2014 36th Annual International Conference of the IEEE Engineering in Medicine and
402 Biology Society, EMBC 2014*.
- 403 [15] Willson, A. M., Richburg, C. A., Czerniecki, J., Steele, K. M., and Aubin, P. M., 2020, "Design and
404 Development of a Quasi-Passive Transtibial Biarticular Prosthesis to Replicate Gastrocnemius Function in
405 Walking," *J. Med. Device.*, **14**(2), p. 025001.
- 406 [16] Fey, N. P., Klute, G. K., and Neptune, R. R., 2012, "Optimization of Prosthetic Foot Stiffness to Reduce
407 Metabolic Cost and Intact Knee Loading During Below-Knee Amputee Walking: A Theoretical Study," *J.
408 Biomech. Eng.*, **134**, pp. 111005-1–10.
- 409 [17] Esposito, E. R., and Miller, R. H., 2018, "Maintenance of Muscle Strength Retains a Normal Metabolic Cost
410 in Simulated Walking after Transtibial Limb Loss," *PLoS One*, **13**(1), pp. 1–19.
- 411 [18] Miller, S., 2020, "Simscape Multibody Contact Forces Library."
- 412 [19] LaPrè, A. K., Price, M. A., Wedge, R. D., Umberger, B. R., and Sup, F. C., 2018, "Approach for Gait
413 Analysis in Persons with Limb Loss Including Residuum and Prosthesis Socket Dynamics," *Int. j. numer.
414 method. biomed. eng.*, **34**(4), p. e2936.
- 415 [20] Jia, X., Zhang, M., and Lee, W. C. C., 2004, "Load Transfer Mechanics between Trans-Tibial Prosthetic
416 Socket and Residual Limb - Dynamic Effects," *J. Biomech.*, **37**, pp. 1371–77.
- 417 [21] De Leva, P., 1996, "Adjustments to Zatsiorsky-Seluyanov's Segment Inertia Parameters," *J. Biomech.*,
418 **29**(9), pp. 1223–1230.
- 419 [22] Wu, G., Siegler, S., Allard, P., Kirtley, C., Leardini, A., Rosenbaum, D., Whittle, M., D'Lima, D. D.,
420 Cristofolini, L., Witte, H., Schmid, O., and Stokes, I., 2002, "ISB Recommendation on Definitions of Joint
421 Coordinate System of Various Joints for the Reporting of Human Joint Motion - Part I: Ankle, Hip, and
422 Spine," *J. Biomech.*, **35**(4), pp. 543–548.
- 423 [23] Grood, E. S., and Suntay, W. J., 1983, "A Joint Coordinate System for the Clinical Description of Three-
424 Dimensional Motions: Application to the Knee.," *J. Biomech. Eng.*, **105**(2), pp. 136–44.

- 425 [24] Thakallapelli, A., Ghosh, S., and Kamalasadana, S., 2016, "Real-Time Frequency Based Reduced Order
426 Modeling of Large Power Grid," *IEEE Power and Energy Society General Meeting*, IEEE Computer
427 Society.
- 428 [25] Kikuchi, R., Misaka, T., and Obayashi, S., 2016, "International Journal of Computational Fluid Dynamics
429 Real-Time Prediction of Unsteady Flow Based on POD Reduced-Order Model and Particle Filter," *Int. J.*
430 *Comput. Fluid Dyn.*, **30**(4), pp. 285–306.
- 431 [26] Webber, C. M., and Kaufman, K., 2017, "Instantaneous Stiffness and Hysteresis of Dynamic Elastic
432 Response Prosthetic Feet," *Prosthet. Orthot. Int.*, **41**(5), pp. 463–8.
- 433 [27] Womac, N. D., Neptune, R. R., and Klute, G. K., 2019, "Stiffness and Energy Storage Characteristics of
434 Energy Storage and Return Prosthetic Feet," *Prosthet. Orthot. Int.*, **00**(0).
- 435 [28] Van Hulle, R., Schwartz, C., Denoël, V., Croisier, J.-L., Forthomme, B., and Brüls, O., 2020, "A
436 Foot/Ground Contact Model for Biomechanical Inverse Dynamics Analysis," *J. Biomech.*, **100**(2020).
- 437 [29] Lopes, D. S., Neptune, R. R., Ambrósio, J. A., and Silva, M. T., 2015, "A Superellipsoid-Plane Model for
438 Simulating Foot-Ground Contact during Human Gait," *Comput. Methods Biomech. Biomed. Engin.*
- 439 [30] Brown, P., and McPhee, J., 2018, "A 3D Ellipsoidal Volumetric Foot–Ground Contact Model for Forward
440 Dynamics," *Multibody Syst. Dyn.*, **42**(4), pp. 447–467.
- 441 [31] Jackson, J. N., Hass, C. J., and Fregly, B. J., 2016, "Development of a Subject-Specific Foot-Ground
442 Contact Model for Walking," *J. Biomech. Eng.*, **138**(9), pp. 091002-1–12.
- 443 [32] Winter, D. A., and Sienko, S. E., 1988, "Biomechanics of Below-Knee Amputee Gait," *J. Biomech.*, **21**(5),
444 pp. 361–367.
- 445 [33] Su, P.-F., Gard, S. A., Lipschutz, R. D., and Kuiken, T. A., 2008, "Differences in Gait Characteristics
446 Between Persons With Bilateral Transtibial Amputations, Due to Peripheral Vascular Disease and Trauma,
447 and Able-Bodied Ambulators," *Arch Phys Med Rehabil*, **89**(7), pp. 1386–1394.
- 448

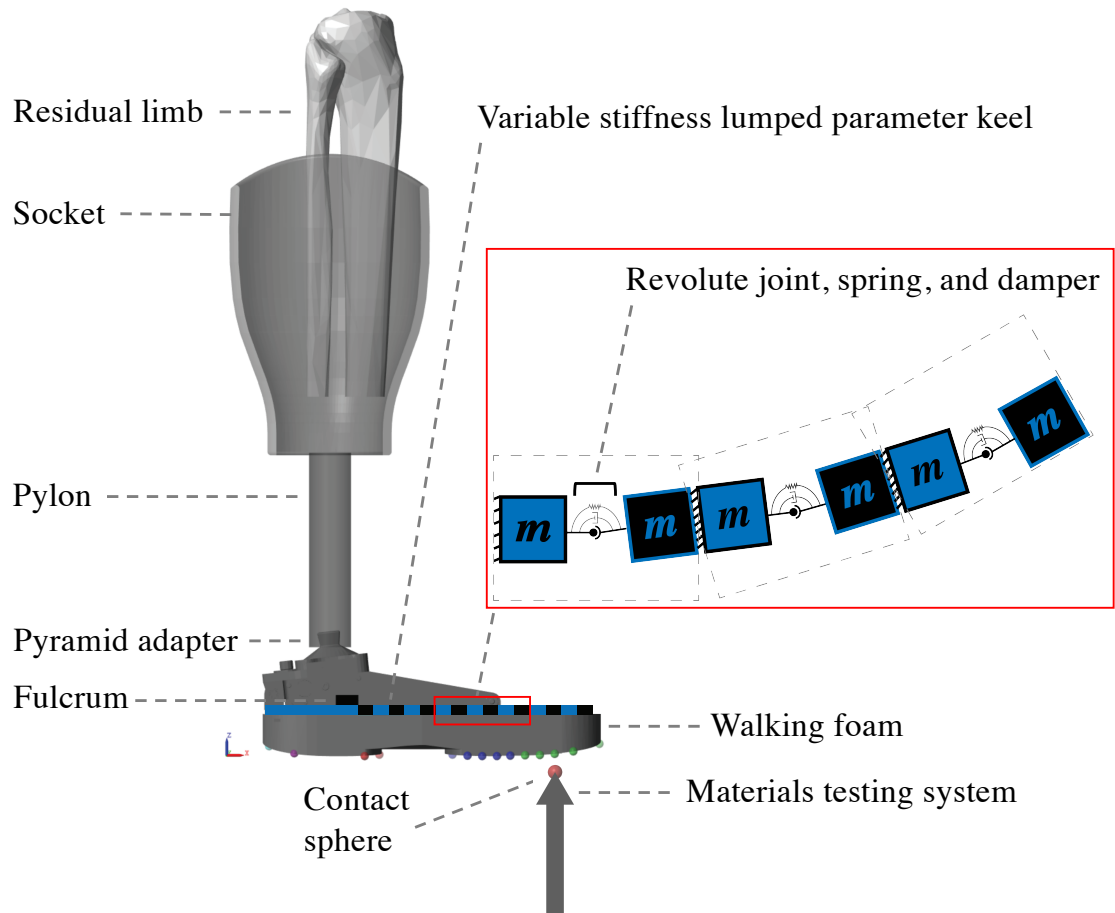
449



450

451 Figure 1: Overhung cantilever beam model of the VSF. The schematic illustrates keel length (L) pinned at A and simply
 452 supported at B, with a force applied at C. Overhung length ($a = L - l$) (supported length). Image reproduced with permission from
 453 Glanzer and Adamczyk (2018).

454

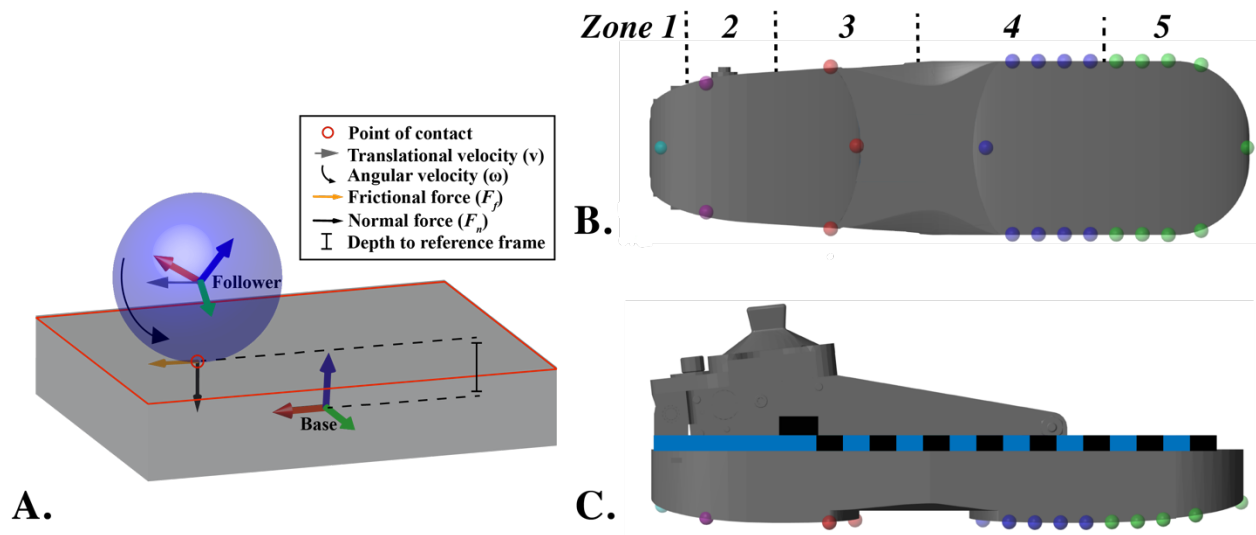


455

456 Figure 2: Modeled VSF, pylon, socket, and materials testing system (MTS). The MTS translates vertically, contacting the VSF
 457 30 mm proximal to the end of the keel (Glanzer and Adamczyk 2018).

458

459



460

461 Figure 3: Schematic of a single sphere-to-plane contact model (A) and contact model plantar (B) and lateral (C) perspectives of
 462 the VSF sphere-to-plane contact models. Heel contact spheres vary in color by zone.

463

464

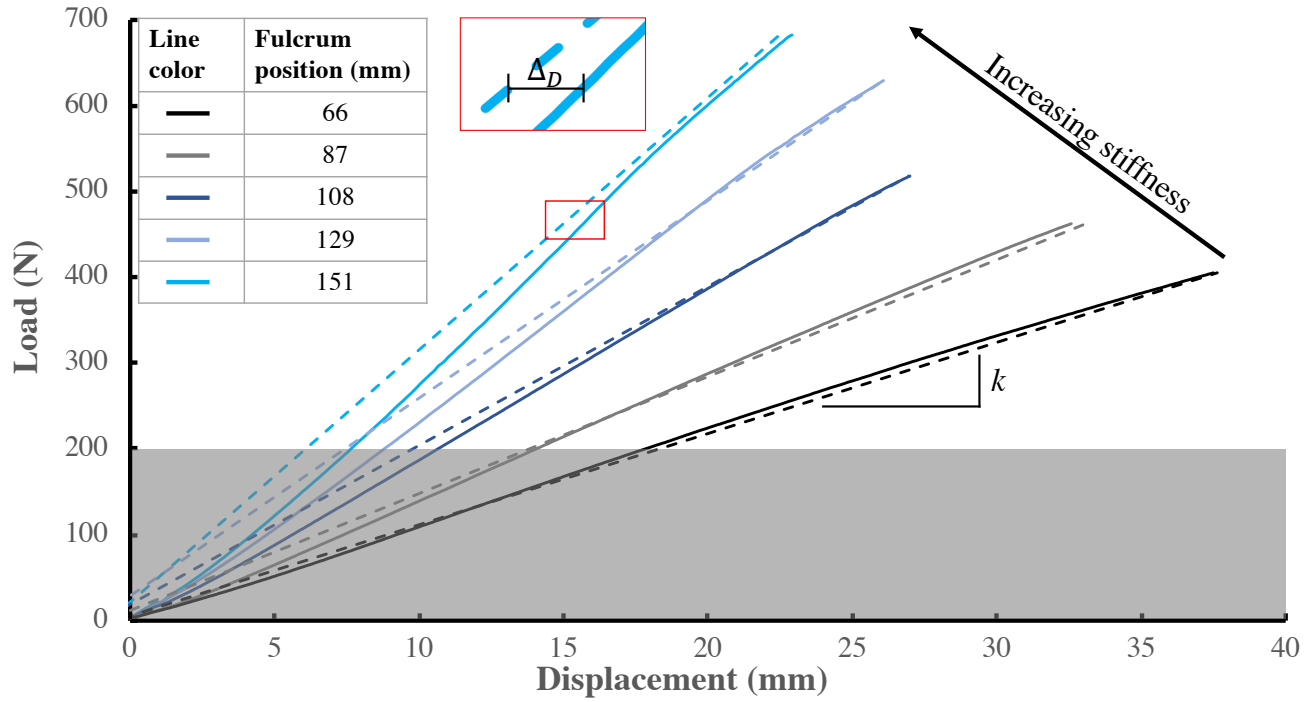
Table 1: Summary of sphere-to-plane contact model parameters for the VSF.

Location	k (N/mm)	b (N·s/mm)	Penetration for full damping (mm)	Penetration exponent
Zone 1	90.16	3.525	7.474	297.7
Zone 2	91.11	390.9	2.000	458.4
Zone 3	18.01	292.9	2.900	3.152
Zone 4	1003	252.1	0.765	0.977
Zone 5	123.8	476.7	1.700	0.754

465

k : stiffness, b : damping

466



467

468 Figure 4: Load-displacement relationships for simulation (dashed) and experimental data (solid). Data are best fit $\pm 95\%$
 469 confidence interval. Displacement offset (Δ_D), example depicted with a bracket (|–|), is the difference between simulated and
 470 experimental mid-range displacement (eq. (3)).

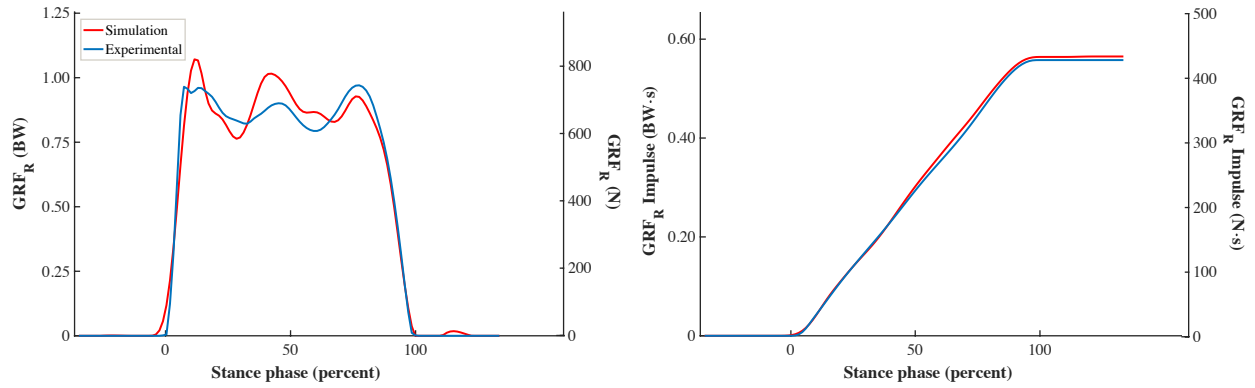
471

472 Table 2: Comparative summary of experimental and simulated stiffness and mid-range displacement.

Fulcrum position (mm)	k_{exp} (N/mm)	k_{sim} (N/mm)	Displacement offset (mm)	
66	10.43 ± 0.07	10.94 ± 0.00	0.02	473
87	14.17 ± 0.08	13.62 ± 0.00	-0.46	474
108	19.45 ± 0.10	18.52 ± 0.00	0.23	475
129	24.83 ± 0.16	23.04 ± 0.00	0.32	476
151	31.59 ± 0.24	29.41 ± 0.00	0.79	477
				478

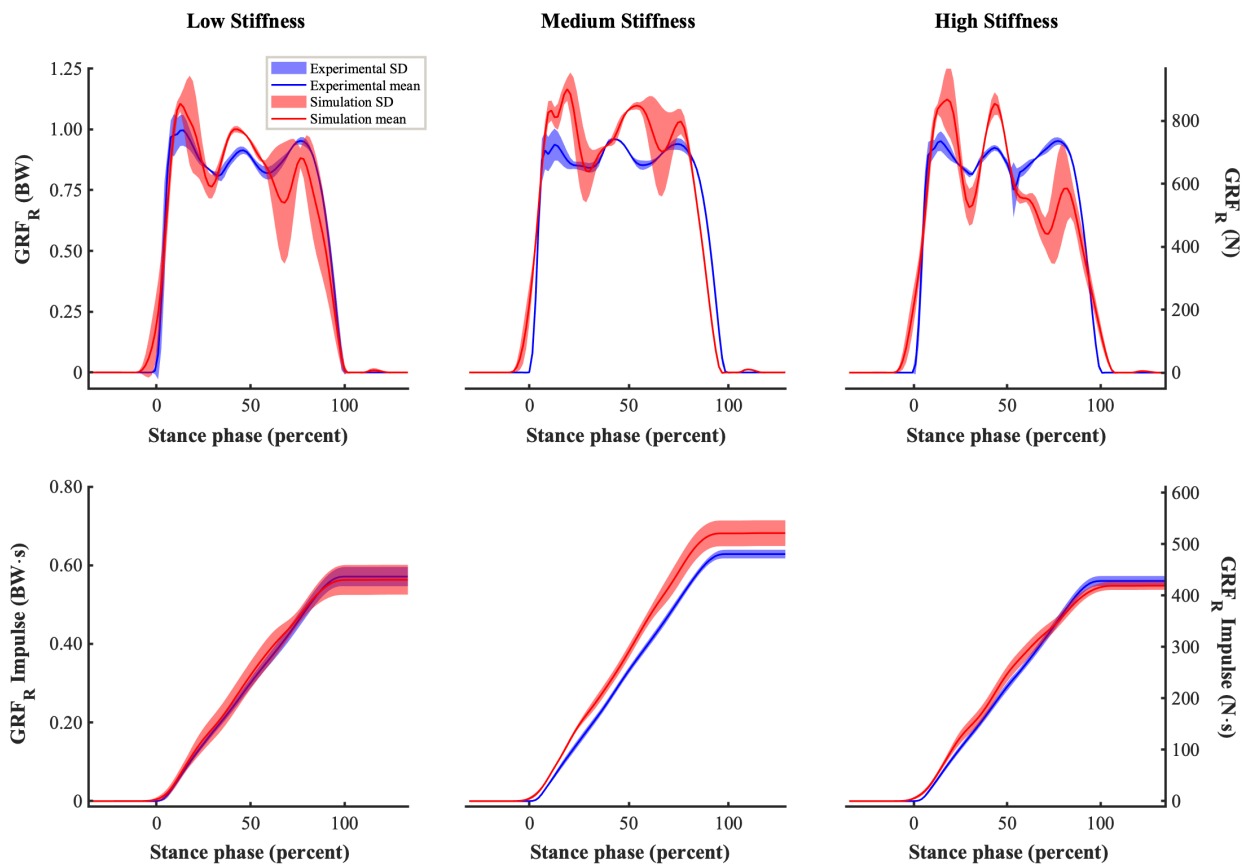
479 Displacement (D) offset: $D_{sim} - D_{exp}$. Data are mean \pm SD.

480



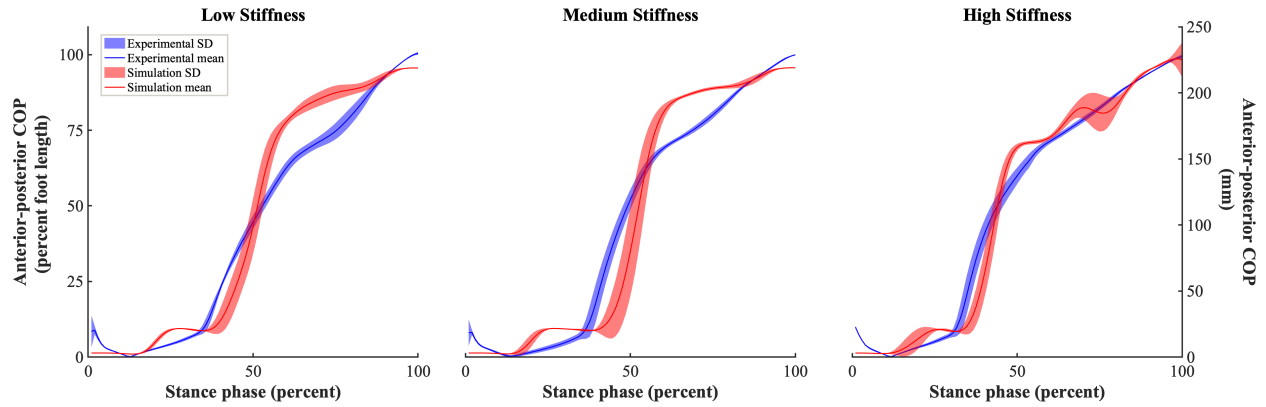
481

482 Figure 5: Optimized GRF_R and GRF_R impulse for a single trial at 66 mm fulcrum position.



483

484 Figure 6: Ensemble curves for GRF_R (top) and GRF_R Impulse (bottom) for the low, medium, and high stiffness conditions (left,
485 middle, and right).



486
487 Figure 7: Ensemble curves for COP_{ap} position for the low, medium, and high stiffness conditions (left, middle, and right).

488
489 Table 3: Summary of GRF_x , GRF_z impulse, and COP_{ap} comparison between simulated and experimental data.

Stiffness Configuration	GRF_x		GRF_x Impulse		COP_{ap}	
	R^2	RMSE (BW)	R^2	RMSE (BW·s)	R^2	RMSE (% FL)
Low	0.93 ± 0.05	0.10 ± 0.04	$> 0.99 \pm 0.01$	0.02 ± 0.01	0.95 ± 0.01	8.93 ± 0.99
Medium	0.92 ± 0.01	0.13 ± 0.02	0.96 ± 0.02	0.05 ± 0.01	0.94 ± 0.01	9.45 ± 0.92
High	0.87 ± 0.07	0.14 ± 0.07	$> 0.99 \pm 0.01$	0.02 ± 0.01	0.97 ± 0.01	5.68 ± 1.39

490 **BW**: Body weight, **COP_{ap}** : Anterior-posterior center of pressure, **FL**: Foot length, Data are mean \pm SD

491